THE JOURNAL OF PHYSICAL CHEMISTRY C
A JOURNAL OF THE AMERICAN CHEMICAL SOCIETY

pubs.acs.org/JPCC

Article

Simple Synthesis of Monodisperse Ultrasmall Au Icosahedral Nanoparticles

Ezgi Yildirim, Raj Kumar Ramamoorthy,* Rohan Parmar, Pierre Roblin, Jorge A. Vargas, Valeri Petkov, Ana Diaz, Stefano Checchia, Isaac Rodriguez Ruiz, Sébastien Teychené, Lise-Marie Lacroix,* and Guillaume Viau*

Cite This: *J. Phys. Chem. C* 2023, 127, 3047−3058

Read Online

ACCESS | Metrics & More | Article Recommendations | Supporting Information

ABSTRACT: Ultrasmall metal nanoparticles (NPs) with a mean diameter below 2 nm are being intensively studied due to their unique structural and chemical properties. At such small sizes, metal particles can appear as various polyhedra with different atomic structures depending on whether electronic effects, surface energy, or the nucleation mechanism govern their crystallization. Therefore, the synthesis of monodisperse nanoparticles of a very small size and well-defined structure requires a good understanding of the different steps of the crystallization process, which can be achieved by conducting and coupling *in situ* studies at different length and time scales. In this article, we describe the synthesis of ultrasmall gold NPs by reduction of $HAuCl_4$ in solution of oleylamine (OY) in hexane using trialkylsilanes as reducing agents. Thanks to time-resolved *in situ* small-angle X-ray scattering and X-ray absorption spectroscopy kinetic studies, a competition between nucleation of Au NPs from a solution containing Au(III) clusters and crystallization of a lamellar phase of composition OY-Au(I)-Cl was revealed. *In situ* X-ray diffraction and pair distribution function (PDF) analysis showed that the first chemical pathway leads to icosahedral NPs while the reduction of OY-Au(I)-Cl leads to *fcc* NPs. Increasing the reaction rate, achieved by adjusting the silane concentration, changing the nature of the silane (triethylsilane instead of triisopropylsilane), and/or increasing the temperature of reaction, avoided the formation of the Au(I) lamellar phase as the intermediate, leading to monodisperse Au NPs with an icosahedral structure. This fairly simple liquid-phase synthesis method yields highly concentrated suspensions of icosahedral gold NPs, paving the way for their future use in practical applications such as catalysis.

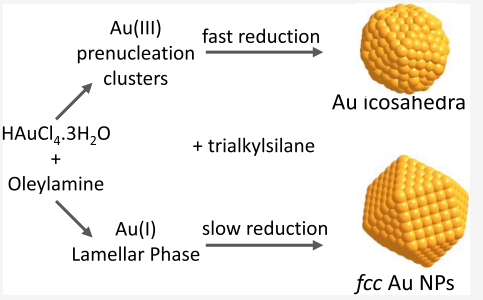

1. INTRODUCTION

Designing nanoparticles (NPs) with well-defined morphology (size and shape) and structure is essential for the advancement of a wide range of enabling technologies.[1] Especially, producing monodisperse metal nanoparticles with a low symmetry crystalline structure is fundamentally[2,3] and technologically important for their superb properties finding use in optical,[4,5] catalytic,[6] and electronics[7,8] applications. Gas-phase synthesis approaches allow producing size-selected clusters with controlled atomic structures, such as icosahedra, decahedra, or bulk structure polyhedra.[9] These approaches are very useful to follow the structure of clusters with different sizes giving unique information on the role of the different synthesis parameters (electronic, surface, or kinetic) involved in the stabilization of the different nanostructures. It is well established that, when produced in the gas phase, icosahedra are energetically favored at small sizes. The critical size below which this structure is favored in the case of gold is generally found to be around 100 atoms even if structural isomers comprising a "magic number" of atoms, such as Au_{561}, Au_{742}, and Au_{923} clusters, were also produced.[10,11] In addition, for a given NP size, the structure can be highly dependent on the atmosphere to which the NPs are exposed.[12,13]

The liquid-phase approaches have the advantage of producing large quantities of NPs in a single batch but the synthesized NPs are generally polydisperse. These methods require the use of stabilizing agents to control the particle size that can strongly affect the stability range of targeted atomic structures.[11,14] At large sizes, NP polymorphs under thermodynamic control can be described by the Wulff construction including the effect of surface ligand in the calculation of the surface energy.[15] Experimentally, using various ligands (amines, acids)[16−18] or polymers,[19] noble-metal nanoparticles exhibiting icosahedral shape, consisting of 20 triangular facets and the 2-fold, 3-fold, and 5-fold symmetry axis,[20] were prepared by liquid-phase chemistry up to large

Received: October 18, 2022
Revised: January 20, 2023
Published: February 6, 2023

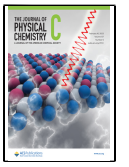

https://doi.org/10.1021/acs.jpcc.2c07323
J. Phys. Chem. C 2023, 127, 3047−3058

sizes (10−90 nm).[21] The atomic structure in these cases is described as a multitwinned face-centered cubic (*fcc*) structure.[22] The XRD pattern of such large icosahedral NPs is close to that of the *fcc* NPs while the XRD signature of ultrasmall icosahedra differs significantly. At small sizes, the symmetry and the interatomic distances are indeed different from the bulk.[22,23]

Achieving control over the size and structure of NPs requires good understanding of the nucleation/growth mechanism, which in turn, requires time-resolved *in situ* studies, such as small- and wide-angle X-ray scattering and X-ray absorption spectroscopy (XAS).[24,21] Generally, the size and size distribution of gold nanoparticles are described by the classical nucleation theory (CNT).[24] According to the CNT, once atoms in solution exceed the solubility limit, they aggregate and form stable nuclei after crossing the energetic barrier imposed by the volume and surface energies. Then, they attach to growing nanoparticles by an atom by atom addition process. The size of the resulting nanoparticles is inversely proportional to the supersaturation ratio, which is defined by the ratio of the actual and equilibrium concentration (or in other words, the solubility limit) of the precursors.[25,26] Nonetheless, using UV−Vis,[27] X-ray scattering,[28] atomic force microscopy,[29] dynamic light scattering,[30] and transmission electron microscopy (TEM),[31] examples of metal nanoparticles grown in solution via one or several non-crystalline intermediate states (such as oligomers, pre-nucleation clusters (PNCs), liquid−liquid phase separation, and amorphous) were revealed. The emergence of non-crystalline structure states during the synthesis of inorganic nanoparticles and their influence on the final structure are well documented.[32] For nanoparticles like $CaCO_3$,[33] YVO_4,[34] and Fe_3O_4,[35] morphologies of non-crystalline intermediate states are found to be reflected in the final morphology of nanoparticles. In addition, the local symmetry of amorphous $CaCO_3$,[36] especially the uncommon metastable vaterite structure, is found to be preserved in the final nanoparticles. In the case of metal nanoparticles, the complexity of the nucleation stage can come from the presence of surfactants introduced in the reaction. These molecules are not only the stabilizing agents of the final particles but can also be ligands of the metal precursors and/or be involved in the structuring of the growth medium. Thus, they may play different roles at different stages of the chemical reaction and have strong effects on the kinetics of the NP formation.

In the synthesis of gold nanoparticles by reduction of a gold precursor in organic solvent containing oleylamine (OY), previous studies showed how the OY/Au molar ratio in the precursor solution affects the shape of the gold particles. Ultrasmall particles and ultrathin nanowires were obtained for [OY]/[Au] of 2.5 and 10−20, respectively.[23] In both cases, *in situ* small-angle X-ray scattering (SAXS) studies revealed that the precursor solution contained pre-nucleation clusters.[37,28] The structural studies combining *in situ* high-energy X-ray diffraction (HE-XRD) and scanning transmission electron microscopy showed in both cases that the particles do not crystallize with a *fcc* structure as expected for bulk Au. Rather, the ultrasmall particles exhibited an icosahedral structure while the ultrathin nanowires crystallized with a structure close the one of α-Mn.[23] In this article, we report the synthesis of ultrasmall Au NPs in the presence of OY and with trialkylsilanes as the reducing agent. Two competitive reaction pathways have been unraveled by *in situ* characterization techniques (ranging from SAXS for length scales from ∼1 to 100 Å to XAS to follow various oxidation states) combined with dedicated microfluidic setups to gain access to short reaction times. Experimental conditions were designed to yield quantitatively monodisperse Au NPs with icosahedral structures using a simple synthesis.

2. EXPERIMENTAL DETAILS

2.1. Au Nanoparticle Synthesis. Hydrogen tetrachloroaurate trihydrate ($HAuCl_4{\cdot}3H_2O$, 99.99%, Alfa Aesar), triisopropylsilane (TIPS, 98%, Sigma-Aldrich), triethylsilane (TES, 99%, Sigma-Aldrich), oleylamine (OY, 80−90%, Acros), and hexane (mixed isomer, 98 + %, Alfa Aesar) were used as received. Syntheses of Au nanoparticles were performed by reduction of $HAuCl_4{\cdot}3H_2O$ by TIPS or TES in solution of OY in hexane. For all syntheses, the final nominal concentration of Au and OY in hexane were kept constant at 20 and 50 mM, respectively, and TIPS and TES concentrations were varied from 62 mM to 1 M. $HAuCl_4{\cdot}3H_2O$ was dissolved in hexane by the addition of OY and sonication, leading to a yellow solution. The vial was placed in a thermostatic bath to control the reaction temperature. A solution of the trialkylsilane in hexane was added rapidly. The reactants were kept undisturbed in the thermostatic bath for 3 h to obtain the final NPs. A color change from yellow to dark red/brown was observed after a certain reaction time, depending on the temperature, the concentration of the reducing agent, and its nature (TIPS or TES). At 25 °C, the color change is observed after 3 min with [TIPS] = 62 mM, whereas it is almost instantaneous with [TIPS] = 1 M or [TES] = 62 mM. Transmission electron microscopy (TEM) samples were prepared by depositing a drop of the colloidal NP suspensions on a copper grid covered with amorphous carbon. The concentration of the colloidal suspension was adjusted by diluting the NPs in hexane. TEM images were recorded using a JEOL 1400 microscope working at 120 kV.

The Au(I) lamellar phase was prepared by adding a sub stoichiometric concentration of TIPS (10 mM) into a solution containing $HAuCl_4{\cdot}3H_2O$ (20 mM) and OY (50 mM). The reaction was left undisturbed at 25 °C for 1 h. The yellow color progressively faded away, and a white precipitate was formed. The white precipitate was recovered by centrifugation (5000 rpm, 5 min) and purified 3 times by addition of hexane and further centrifugation. The product was finally dried under vacuum resulting in a white paste further analyzed by conventional chemical analysis, X-ray photoelectron spectroscopy (XPS), and X-ray diffraction.

2.2. Microfluidic Setup. In order to follow precisely the gold speciation by XAS and the scattering signal by SAXS as a function of time, a homemade hybrid Kapton-OSTEMER (Mercene Labs, Sweden) microfluidic cell has been fabricated according to procedures described elsewhere.[38,39] The structure is described in details in the Supporting Information (Figure S1). It comprises two inlets for reagent injection coupled to an ultrafast mixer with a butterfly-shape structure adapted from the literature.[40] Subsequently, the interrogation channel is conceived with a cross section adapted ad hoc for the specific characterization technique (370 μm × 200 μm for SAXS and 2 × 2 mm for XAS). The cell can operate as a continuous flow reactor by continuously injecting the reagent solutions or as a stop-flow cell probing both short and long reaction times.

2.3. SAXS. Small-angle X-ray scattering of the final NP suspensions was performed on a XEUSS 2.0 laboratory

https://doi.org/10.1021/acs.jpcc.2c07323
J. Phys. Chem. C 2023, 127, 3047−3058

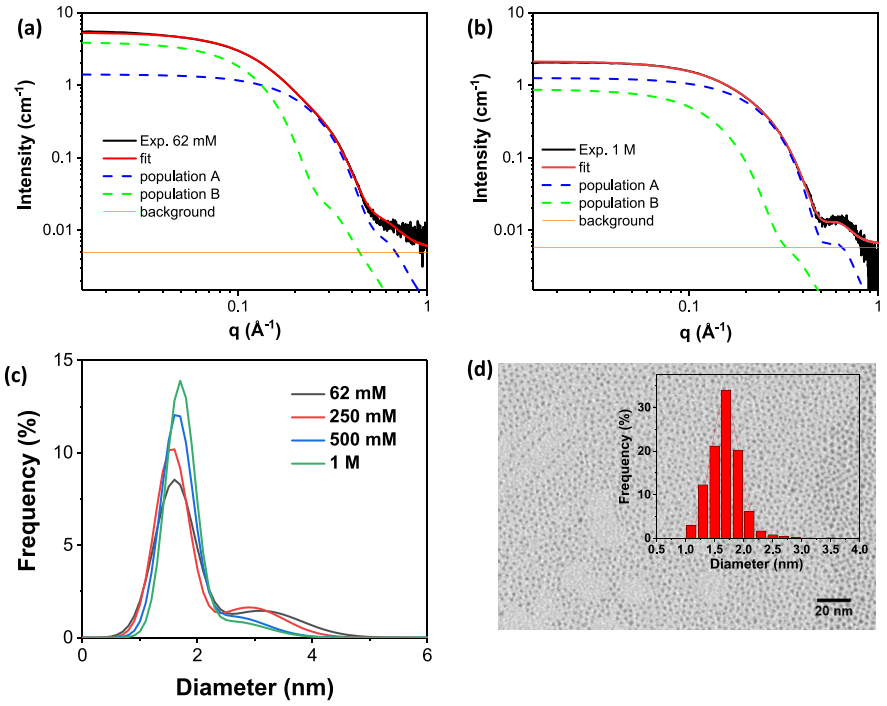

Figure 1. SAXS patterns of suspensions of Au nanoparticles obtained after 3 h of reaction of $HAuCl_4{\cdot}3H_2O$ in OY/hexane ([Au] = 20 mM; [OY] = 50 mM) using TIPS as the reducing agent, in different concentrations: (a) [TIPS] = 62 mM and (b) [TIPS] = 1 M. In black: experimental data; red: the corresponding fit considering two populations of nanospheres (blue and green dashed lines) and a constant background (orange); (c) volume-weighted distribution determined from the fit of the *in situ* SAXS of the final Au NPs obtained after 3 h of reaction with different TIPS concentrations; (d) TEM image of Au nanoparticles obtained after 3 h of reaction at T = 25 °C with [TIPS] = 1 M. Inset: the corresponding number-weighted size distribution determined from the image analysis.

instrument equipped with a pixel detector PILATUS 1M (DECTRIS) and a Cu Kα X-ray source provided by GeniX3D (λ = 1.54 Å). The sample to detector distance was fixed to record the SAXS signal in the q range 0.015−1 Å^{-1}. The SAXS signals of the Au NPs were analyzed using SaSView 5.0.4. A summation of two form factors of the Au nanosphere presenting a polydispersity was used to fit the experimental data. The scattering length densities of 126 × 10^{-6} and 6.1 × 10^{-6} Å^{-2} were taken for Au and hexane, respectively. The relative scale of the two form factors, radii and polydispersity, and the incoherent contribution (background intensity) were adjustable parameters. Time-resolved *in situ* SAXS experiments were carried out at the c-SAXS beamline at the Swiss Light Source, Paul Scherrer Institute (PSI) in Villigen (Switzerland). SAXS signals, during the crystallization of gold nanoparticles, were recorded using the aforementioned microfluidic chip in continuous and stopped flow configurations. X-rays with an energy of 11.5 keV and beam size of 30 μm × 50 μm (vertical × horizontal) were incident on the sample in transmission mode. The scattered X-ray intensities were recorded at a distance of 2.17 m using a PILATUS 2M detector giving a q range from to 0.01 to 0.7 Å^{-1}. The reactions were followed between 4 s and 30 min every 1 s.

2.4. XAS. Time-resolved *in situ* X-ray absorption spectroscopy (XAS) experiments were carried out at the SuperXAS beamline (PSI, Switzerland). XAS was conducted at the Au L_{III}-edge in fluorescence mode. Like SAXS studies, time-resolved XAS signals were collected in the two configurations: in continuous flow, the XAS signal was captured between 1 s and 30 s every 0.1 s; in stopped flow, the XAS signal was recorded until the end of a reaction every 3 or 4 s. The time-resolved XANES spectra were analyzed by linear combination analysis (LCA) of three spectra used as references for the Au(III), Au(I), and Au(0) oxidation states, which were, respectively, the precursor solution obtained by dissolving $HAuCl_4{\cdot}3H_2O$ in the solution of oleylamine in hexane, the OYAu(I)Cl lamellar phase, and the final Au NPs. This method provided an assessment of the gold speciation as a function of time. More details are given in the Supporting Information.

2.5. HE-XRD, PDF, and Modeling. High-energy X-ray diffraction data were collected at the ID15A beamline (ESRF, France).[41] For HE-XRD, an X-ray beam with an energy of 69 keV (λ = 0.1797 Å) was incident on a 1.5 mm diameter capillary containing the nanoparticles in suspension in the mother liquor. The X-ray scattering patterns were recorded using a Pilatus 2M detector in the q range from 0.2 to 22 Å^{-1}. Based on TEM and SAXS data for NP size and morphology, several real NP size and shape models were prepared starting from known structures. The models were relaxed by molecular dynamics using a potential for gold[42] from the modified embedded atom method as implemented in LAMMPS.[43] The pair distribution functions (PDF), $G(r)$, were obtained from these models and compared with the experimental one. The best candidate models were further refined against experimental PDF data using reverse Monte Carlo simulations, following a protocol described in ref 44.

3. RESULTS AND DISCUSSION

3.1. Influence of the TIPS Concentration. Several batches of Au nanoparticles were prepared by the reduction of $HAuCl_4{\cdot}3H_2O$ in solution of oleylamine in hexane using different concentrations of TIPS, which serves as the reducing agent. The stoichiometry of the reaction is

https://doi.org/10.1021/acs.jpcc.2c07323
J. Phys. Chem. C 2023, 127, 3047−3058

Table 1. Summary of the Adjustable Parameters of the Two Gaussian Distributions (A and B) Used to Fit the Experimental SAXS Pattern of Au Nanoparticle Suspensions Obtained after 20 min or 3 h of Reaction Using Different Reaction Parameters: The Mean Diameter, d_m, the Polydispersity Expressed as σ/d_m, (with σ the Standard Deviation of the Gaussian Distribution), and the Relative Volume Fraction of Both Populations, % vol

			SAXS results					
			population A			population B		
experimental conditions for the Au NPs synthesis			d_m	σ/d_m	% vol	d_m	σ/d_m	% vol
[TIPS] effect for T = 25 °C	62 mM	20 min	1.8	0.09	77	2.6	0.24	23
		3 h	1.8	0.17	64	3.5	0.15	36
	250 mM	3 h	1.6	0.19	75	2.9	0.21	25
	500 mM	3 h	1.6	0.17	83	2.6	0.23	17
	1 M	20 min	1.7	0.16	92	2.0	0.48	8
		3 h	1.7	0.15	87	2.6	0.23	13
temperature effect for [TIPS] = 62 mM	25 °C	3 h	1.8	0.17	64	3.5	0.15	36
	30 °C	3 h	1.9	0.14	70	3.3	0.17	30
	35 °C	3 h	1.9	0.14	85	3.4	0.15	15
	40 °C	3 h	2.0	0.11	92	3.8	0.10	8
effect of TES T = 25 °C	62 mM	3 h	2.0	0.08	89	3.5	0.08	11

$$HAuCl_4 + \frac{3}{2}R_3SiH + \frac{5}{2}C_{18}H_{35}NH_2 \rightarrow Au(0) + \frac{3}{2}R_3SiCl + \frac{5}{2}C_{18}H_{35}NH_3^+Cl^- \quad (1)$$

In a first set of experiments, the Au concentration was kept constant at 20 mM, the molar ratio [OY]/[Au] was 2.5, which corresponds to the stoichiometry of eq 1, and the TIPS concentration was varied from 62 mM to 1 M, *i.e.*, from a slight to a large excess compared to the stoichiometry. In every reaction, the yellow color of the precursor solution turned to dark red/brown with the onset of the Au particle formation in suspension. The time at which the solution turned red was strongly dependent on the TIPS concentration: around 180 s for [TIPS] = 62 mM, only a few seconds for [TIPS] = 1 M.

The colloidal suspensions were characterized *in situ* by SAXS after 3 h of reaction (Figure 1a,b and Figure S2). For [TIPS] = 62 mM (Figure 1a) and 250 mM (Figure S2a), a two-step curve was observed, indicating the presence of a bimodal distribution of nanospheres. At higher TIPS concentration, the curves appeared smooth (Figure S2b) and a first oscillation at high q was observed for [TIPS] = 1 M (Figure 1b). All the experimental curves were nicely fitted considering two Gaussian distributions: a major one (henceforth referred to as population A) with a mean diameter of 1.7 ± 0.1 nm, almost independent of the TIPS concentration, and a second one (population B) with a larger diameter (2.6 nm or more). The mean size, d_m, and the relative standard deviation, σ/d_m, are given in Table 1. The relative volume proportion between these two populations depends on the TIPS concentration, as shown in Figure 1c. The proportion of the smallest nanoparticles (population A), *i.e.*, with a mean diameter of less than 2 nm, increased significantly with the concentration of TIPS from 64% for [TIPS] = 62 mM to 87% for [TIPS] = 1 M.

TEM images of the different samples showed ultrasmall particles with a diameter of less than 2 nm. A representative TEM image of particles prepared with [TIPS] = 1 M is given in Figure 1d. The image analysis revealed a mean diameter of 1.8 ± 0.1 nm and a σ/d_m = 14% determined from the number-weighted size distribution, which reflects the polydispersity of the NPs. These results were in good agreement with the SAXS data. However, larger particles (d > 10 nm) were also observed on the TEM images (Figures S3 and S4). The size of these large particles was well above the size of the particles observed by SAXS. The presence of such large particles in the colloidal suspensions should have produced a signal at small q on the SAXS signal, which was never observed. This is likely due to the very small volume fraction of these large particles. Their relative amount can be overestimated by TEM because of sampling issues in the preparation of the TEM grids. The other reason could be a modification of the particle size morphology when drying the suspensions for *ex situ* TEM observations. The ultrasmall size of the NPs makes them very reactive and thus prone to aggregation and/or recrystallization onto the TEM grid. Therefore, *in situ* SAXS was preferred to unambiguously reveal the effect of the experimental conditions on the Au nanoparticle size distribution.

3.2. *In Situ* SAXS Kinetic Studies. *In situ* SAXS experiments were carried out to follow the reduction of the gold precursor into Au NPs at different TIPS concentrations. Figure 2 depicts the time variation of the *in situ* SAXS patterns recorded during the synthesis of nanoparticles with the TIPS concentrations of 62 mM and 1 M.

Scattering objects were detected in the precursor solution before the addition of TIPS. A mean size of around 4 nm was determined using the Beaucage model.[45] These scattering objects were interpreted as pre-nucleation clusters (PNCs) containing Au(III) complexes, which are formed by the dissolution of $HAuCl_4 \cdot 3H_2O$ in hexane thanks to the presence of OY.[28] After the addition of TIPS, the scattering intensity remained fairly constant during a given period of time referred to as the induction stage. The duration of this stage varies with the TIPS concentration: ∼15 s for [TIPS] = 1 M and up to ∼180 s for [TIPS] = 62 mM. We previously reported that, during this induction stage, the Au(III) complexes are partially reduced into Au(I) without any changes in the PNC size.[28] At the end of this induction stage, the "knee-position" of the scattering intensity profiles shifted toward the high q, revealing a decrease of the scattering objects' mean size. The shift was very fast with the highest TIPS concentration (Figure 2a) and more progressive for lower concentration (Figure 2b). This shift was interpreted as the onset of the small Au nanoparticles in the medium, *i.e.*, the beginning of the nucleation. These small particles strongly scatter X-rays compared to PNCs and become predominant in the SAXS signal. For [TIPS] = 1 M,

https://doi.org/10.1021/acs.jpcc.2c07323
J. Phys. Chem. C 2023, 127, 3047−3058

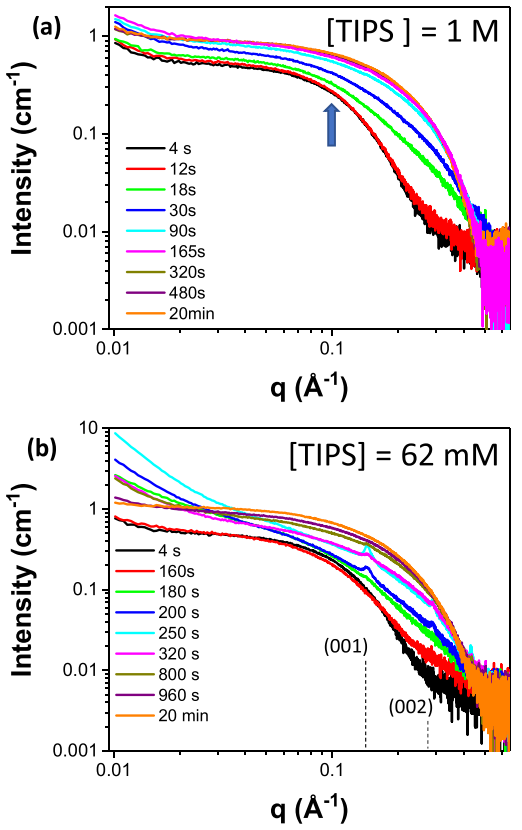

Figure 2. Time-resolved *in situ* synchrotron SAXS patterns recorded during the synthesis of Au nanoparticles in OY/hexane solution with different TIPS concentrations: (a) [TIPS] = 1 M (the arrow indicates the "knee-position" on the SAXS at 4 s. The knee is shifted to high q after 18 s; (b) [TIPS] = 62 mM. Dashed lines point the (00l) peaks of a lamellar phase with an interlayer distance d_{001} = 43.5 Å.

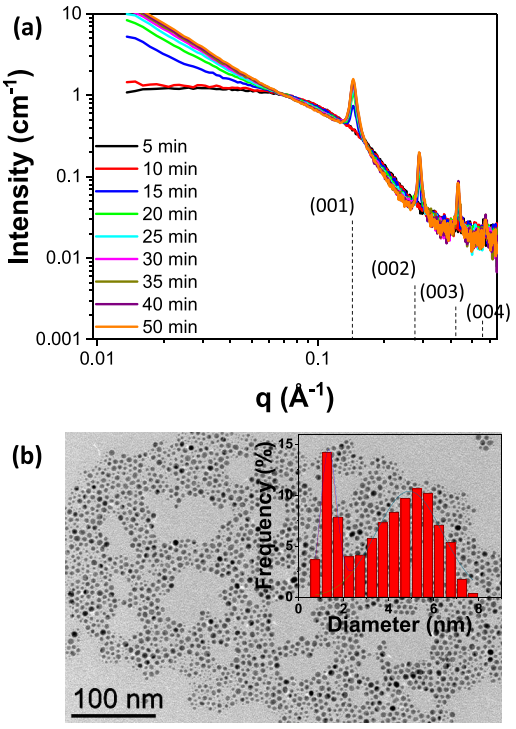

Figure 3. (a) *In situ* SAXS patterns recorded during the partial reduction of $HAuCl_4$ using 0.5 equiv of TIPS at 25 °C (the dashed lines correspond to the (00l) peaks of a lamellar phase with an interlayer distance d_{001} = 43.5 Å); (b) TEM image of Au nanoparticles prepared by reduction of the lamellar phase OYAu(I)Cl with [TIPS] = 1 M. Inset: number-weighted size distribution determined from the TEM image analysis.

the SAXS signal was found constant after ∼4 min (Figure 2a), which can be interpreted as the end of the nucleation and the growth stages.

The SAXS signal varied more progressively for [TIPS] = 62 mM throughout the 20 min of *in situ* measurements (Figure 2b) and still slightly evolved up to 3 h of reaction showing a slower particle growth (Tab. 1). In addition, Bragg peaks at q_1 = 0.1445 Å^{-1} and q_2 = 0.289 Å^{-1} were clearly observed for [TIPS] = 62 mM, along with an increased intensity at small q (Figure 2b), while nothing similar was detected for [TIPS] = 1 M (Figure 2a). The Bragg peaks are interpreted as the crystallization *in situ* of a lamellar phase with an interlayer distance d_{001} = 43.5 Å. The high intensity at low q reveals the formation of large objects constituting the lamellar phase. The onset of the lamellar phase occurred quasi simultaneously with the Au NP nucleation, then was observed from 200 to 800 s, and then vanished (Figure 2b).

3.3. Characterization and Influence of the Intermediate Lamellar Phase. The lamellar phase, which appears during the synthesis with [TIPS] = 62 mM, was isolated to understand its role in the formation of the Au NPs. The gold precursor was reduced with TIPS, which was deliberately limited to a sub-stoichiometric concentration, *i.e.*, 10 mM, to avoid the formation of metallic particles. According to eq 1, the reaction of 20 mM Au(III) with 10 mM TIPS is indeed expected to give a mixture of 50% Au(III) and 50% Au(I). The reaction was followed *in situ* by SAXS (Figure 3a). Up to 10 min, the characteristic signal of PNCs was observed. After about 12 min, the (00l) Bragg peaks appeared, exhibiting the same interlayer distance of 43.5 Å as the *in situ* SAXS of the NP synthesis with 62 mM of TIPS. The intensity at low q values increased with time, concomitantly with the Bragg peaks' intensities. After 50 min of reaction, the SAXS pattern did not further evolve, indicating a fairly stable lamellar phase (Figure S5). The white precipitate was then isolated by centrifugation, washed several times with hexane to remove the excess of Au(III) precursors, and then dried under vacuum at room temperature. The combined chemical and XPS analysis of the lamellar phase were in agreement with a Au(I) phase of chemical formula OY-Au(I)-Cl (Table S1), similar to the Au(I) phase reported previously.[46,47]

The direct reduction of the OY-Au(I)-Cl phase, once redispersed in hexane, was carried out with a large excess of TIPS. The concentration of Au and TIPS in the mixture was 20 mM and 1 M, respectively, as in the direct nanoparticle synthesis. The color change, which is a good indicator of the reduction of Au precursor to Au(0) NPs, was observed after about 10 min instead of the ∼15 s needed when starting classically from the Au(III) PNC precursor. Figure 3b shows a representative TEM image of the NPs obtained after 3 h of reaction, revealing much larger NPs, up to 7 nm, with a very broad size distribution (Figure 3b). This clearly shows that, during the NPs synthesis, the OY-Au(I)-Cl intermediate slows down the reduction and favors the growth of the largest NPs. Another experiment confirmed this conclusion. The reduction of $HAuCl_4 \cdot 3H_2O$ (20 mM) dissolved in a solution of OY (50 mM) in hexane was carried out using TIPS in the stoichiometric ratio (30 mM) according to eq 1. The solution

https://doi.org/10.1021/acs.jpcc.2c07323
J. Phys. Chem. C 2023, 127, 3047−3058

became cloudy brown 5 min after the addition of TIPS, indicating the formation of the intermediate lamellar phase concomitantly with the formation of small Au NPs, and dark brown after 8 min. After 3 h of reaction, the TEM images revealed particles with a broad size distribution and mean size of 5.6 nm (Figure S6). Thus, to obtain ultrasmall monodisperse Au, one should avoid the formation of the OY-Au(I)-Cl lamellar phase.

3.4. Parameters for the Optimization of Monodisperse Ultrasmall Au NPs. Since the Au(I) intermediate solid phase was not detected in presence of [TIPS] = 1 M, *i.e.*, for fast reactions, we decided to prevent the formation of OY-Au(I)-Cl by increasing the reduction rate through adjusting the reaction temperature and strength of the reducing agent.

3.4.1. Influence of Temperature. Figure 4a and Figure S7 show the SAXS patterns of the as-prepared Au nanoparticle suspensions after 3 h of reaction obtained in the presence of [TIPS] = 62 mM at different temperatures. The two-step curves indicating the presence of a bimodal distribution of nanospheres progressively smoothened with increasing temperature. At 40 °C, the oscillations at high q, characteristic of fairly monodisperse NPs, were observed (Figure 4a). The fit of the experimental patterns using two populations of nanospheres revealed that the smallest nanoparticles (population A), *i.e.*, with a mean diameter of 2 nm, were indeed favored at higher temperature, reaching more than 90% for T = 40 °C (Table 1, Figure 4b). Thus, even if the temperature was varied in a small range, from 25 to 40 °C, it has a strong effect on the size distribution of the particles.

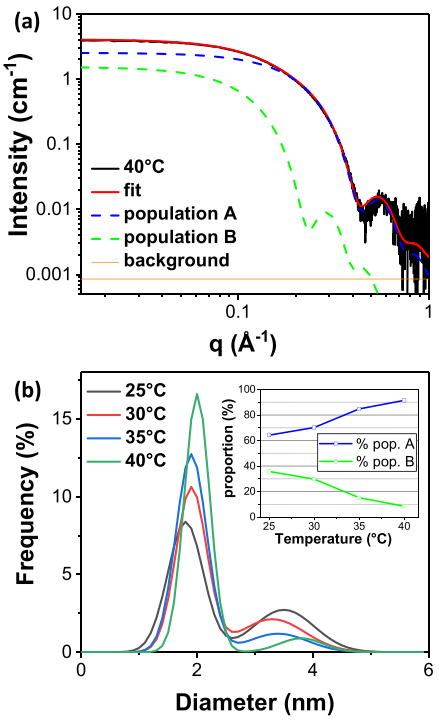

Figure 4. (a) SAXS patterns of suspensions of Au nanoparticles prepared by reduction of $HAuCl_4 \cdot 3H_2O$ in OY/hexane ([Au] = 20 mM ; [OY] = 50 mM) at T = 40 °C using TIPS as the reducing agent ([TIPS] = 62 mM). Black: experimental data; red: best fits including two populations of nanospheres, population A (dashed blue) d_m = 1.8−2 nm; population B (dashed green) d_m = 3.3−3.8 nm; and a constant background (orange). (b) Volume-weighted size distribution determined by SAXS of the particles prepared at different temperatures. Inset: relative proportion of the two populations A and B *vs* reaction temperature.

The increase of temperature from 25 to 40 °C decreased the time at which the solution turned red from 180 to 60 s. Temperature has also an effect on the Au(I) intermediate. The partial reduction of 20 mM $HAuCl_4$ with 10 mM TIPS was performed at T = 40 °C following the same protocol as in the previous section. Interestingly, SAXS recorded *in situ* did not show any Bragg peaks but only an increase of the intensity at small q (Figure S8). Thus, increasing the reaction temperature by only 15 °C accelerates the reduction and prevents the crystallization of the lamellar phase.

3.4.2. Influence of Trialkylsilane. While TIPS is the most commonly used silane for the synthesis of gold nanowires, other silanes have been used for gold nanoparticles[48] or ultrathin copper nanowires synthesis.[49] Keeping the same experimental conditions as before ([Au] = 20 mM; [OY] = 50 mM), Au NP syntheses were carried out at T = 25 °C using triethylsilane (TES) as the reducing agent. As the ethyl chains of TES are less bulky than the isopropyl chains of TIPS are, a lower steric hindrance was expected, which could favor the coordination to the gold complexes and therefore increase the reduction rate. With [TES] = 62 mM the solution turned red only a few seconds after the addition, much faster than the ∼3 min observed with [TIPS] = 62 mM. Au(0) NPs were formed very quickly, supporting our assumption on the higher reactivity of TES. The NPs obtained after 3 h of reaction were characterized by SAXS (Figure 5a). Oscillations were clearly observed, evidencing the large proportion of small NPs (∼ 90%) and their monodisperse character (σ/d_m = 8%, Table 1).

To have a better assessment of the successive reduction steps and understand the difference between the two reducing agents, the Au NPs' syntheses were followed *in situ* by X-ray absorption spectroscopy (XAS). The time-resolved XAS spectra (Figure S9a) were fitted by a linear combination (LCA) of three components: Au(III), Au(I), and Au(0) (Figure S9b), as described in a previous study.[28] Figure 5b,c shows the time variation of the gold speciation, determined by the LCA, during the nanoparticle synthesis in the presence 62 mM TIPS and TES, respectively.

In Figure 5b, three stages can be clearly distinguished. For t < 175 s, an induction stage was observed during which Au(III) is partially reduced to Au(I). At 175 s, the relative concentrations of Au(III) and Au(I) are both around 50%, and the second stage began with the onset of Au(0). This stage lasted around 75 s during which a steep increase of Au(0) up to ∼40% of the gold species was observed. This stage is interpreted as the Au(0) NP nucleation stage and the beginning of growth. From 250 s onward, a third step was observed. The growth rate of Au(0) and the reduction rate of Au(III) decreased sharply compared to the previous step while the concentration of Au(I) species remained fairly constant around 15% in the time interval of 600 s shown in Figure 5b. It then slowly decreased with time. The comparison with the SAXS patterns recorded in the same conditions (Figure 2b) shows that the lamellar phase OY-Au(I)-Cl appears when the concentration of Au(I) ions is at its maximum (50% on the XAS curve). SAXS showed that once formed, the lamellar phase remained in the medium till 800 s, in agreement with the fairly stable relative Au(I) concentration found in XAS. SAXS and XAS showed that the lamellar phase and the Au(0) NPs appear at the same time in the suspension. The nucleation and

https://doi.org/10.1021/acs.jpcc.2c07323
J. Phys. Chem. C 2023, 127, 3047−3058

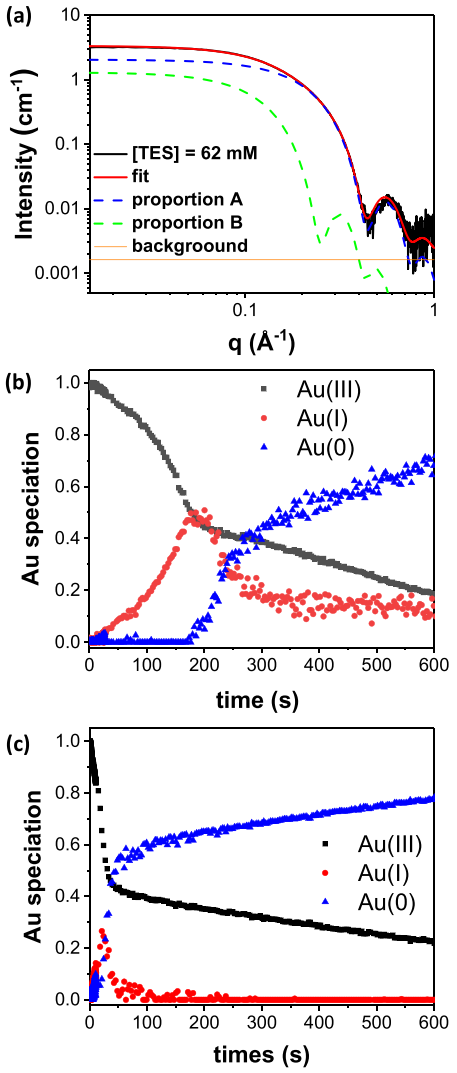

Figure 5. (a) SAXS pattern of Au nanoparticles prepared at 25 °C using TES as the reducing agent ([TES] = 62 mM); (b, c) relative Au(III), Au(I), and Au(0) concentrations deduced from the linear combination analysis of the XAS spectra measured *in situ* during the reaction using (b) [TIPS] = 62 mM and (c) [TES] = 62 mM as the reducing agent.

growth of the gold particles are therefore in competition with the crystallization of the OY-Au(I)-Cl phase. With time, the reduction of the Au(I) species leads to the dissolution of the lamellar phase.

When TES was used as a reducing agent, the same sequence of the three successive stages was observed (Figure 5c), with however significant differences compared to the reduction with TIPS. The induction and the nucleation stages were much shorter, around 12 and 30 s, respectively. The concentration of the Au(I) species reached also a maximum value at the Au(0) onset, *i.e.*, at the beginning of the nucleation stage, but this value was lower than with TIPS, 25% vs 50%. Finally, during the nucleation stage, the concentration of Au(I) tends rapidly to 0, which was not the case with TIPS. Then, [Au(I)] remained equal to zero all over the growth stage while [Au(III)] and [Au(0)] varied almost linearly. If we consider a simple model with two successive reduction steps: Au(III) → Au(I) → Au(0), the low concentration of Au(I) observed in the gold speciation with TES shows that the reduction of Au(I) is much faster than that of Au(III). The intermediate OY-Au(I)-Cl complex cannot crystallize and thus do not interfere with the Au(0) NP nucleation and growth. On the contrary, the slower reduction with TIPS makes possible the crystallization of the OY-Au(I)-Cl lamellar phase.

3.5. Structural Studies on the Final Au NPs. The X-ray diffraction (XRD) patterns of the different Au nanoparticles were measured as prepared, in the mother liquor. Figure 6a shows representative *in situ* XRD patterns of the ultrasmall particles exhibiting a narrow size distribution, *i.e.*, the particles prepared at 25 °C with [TES] = 62 mM or [TIPS] = 1 M and at 40 °C with [TIPS] = 62 mM. The diffraction peaks were very broad as expected for particles with such size but clearly revealed a crystalline structure different from the bulk *fcc* Au.

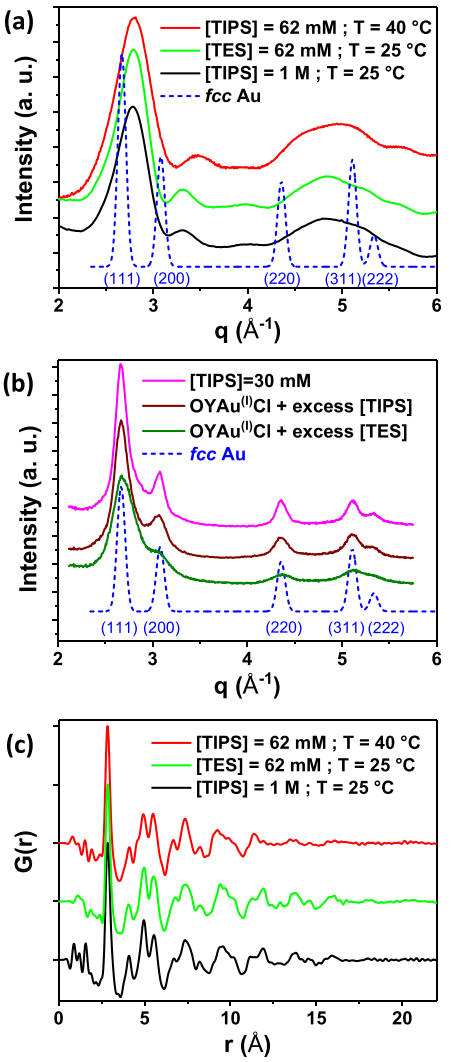

Figure 6. (a) *In situ* HE-XRD Au NPs prepared at T = 25 °C with [TES] = 62 mM (green line), [TIPS] = 1 M TIPS (black line), or at 40 °C with [TIPS] = 62 mM (red line); (b) XRD pattern of Au NPs prepared using the stoichiometric amount of TIPS (30 mM) and by the direct reduction of the lamellar phase OY-Au(I)-Cl with a large excess of TIPS or TES; (c) $G(r)$ oscillations of the Au NPs prepared at T = 25 °C with [TES] = 62 mM (green line), [TIPS] = 1 M TIPS (black line) or at 40 °C with [TIPS] = 62 mM (red line). (a, b): $q = \frac{4\pi \sin\theta}{\lambda}$ and the blue dashed line corresponds to the theoretical XRD pattern of *fcc* Au with an arbitrary peak broadening.

https://doi.org/10.1021/acs.jpcc.2c07323
J. Phys. Chem. C 2023, 127, 3047−3058

The main peak found at q = 2.795 Å^{-1} is shifted to high q values compared to the expected (111) peak of *fcc* Au (q = 2.668 Å^{-1}). An additional feature at 3.3−3.5 Å^{-1} is also observed appearing far away from the (*hkl*) peaks of *fcc* Au (Figure 6a). Figure 6b shows the XRD pattern of the particles prepared with the stoichiometric concentration of TIPS (30 mM) and by the direct reduction of the lamellar phase OY-Au(I)-Cl with a large excess of TIPS (1 M) or TES (1 M). The broadening of the peaks depends on the experimental conditions of synthesis but for all these particles the XRD pattern is consistent with the *fcc* crystal structure of gold. One can conclude that the lamellar phase OY-Au(I)-Cl as the precursor or as the intermediate favors the *fcc* structure.

The ultrasmall particles were analyzed in more detail thanks to high-energy XRD (HE-XRD) and structure modeling. At first glance, the XRD patterns of the ultrasmall particles of Figure 6a look alike but some fine differences can be noted depending on the synthesis conditions. For the particles prepared at 40 °C, the peaks are broader and the second peak is shifted to q = 3.48 Å^{-1} from the value of q = 3.31 Å^{-1} recorded for the two samples prepared at 25 °C (Figure 6a). In order to describe the atomic structure of the ultrasmall Au NPs in more detail, the *in situ* HE-XRD patterns of these three samples were transformed into atomic PDFs (Figure 6b). The physical oscillations in the PDF of the two samples prepared at 25 °C (with [TES] = 62 mM or [TIPS] = 1 mM) extend in the r-space to a distance of about 1.7 nm, which may be considered as a length of structural coherence for the studied NPs. Notably, it appears close to the mean NP diameter measured by SAXS, confirming the good crystallinity of the NPs. On the other hand, the oscillations of the PDF for the sample prepared at 40 °C with [TIPS] = 62 mM appear damped to zero at smaller r values, indicating a reduced coherent length of about 1.3 nm, which is below the 2.0 nm mean size determined by SAXS, indicating an increased level of structural disorder.

To unveil the atomic structure of Au NPs, the *in situ* atomic PDFs were first compared with theoretical PDFs for two clusters containing 309 atoms (1.7 nm in diameter): a cuboctahedron with the *fcc* structure (CBO) and an icosahedron (ICO) (Figure 7 and Figure S10). For reference, a CBO is a *fcc* polyhedra exhibiting six equal squares and eight equal triangles as faces. On the other hand, ICO has 20 triangles as faces and exhibits 5-fold axes, which is a non-crystallographic symmetry. The comparison clearly revealed that the CBO does not reproduce the experimental PDF (Figure 7, top), showing that the NPs have an atomic structure different from that of bulk *fcc* Au. In contrast, the PDF of a perfect ICO with 309 atoms reproduces the experimental data reasonably well (Figure 7, middle). To improve the agreement with the experimental data, a model of a distorted ICO was built by adding a layer of atoms to some of the NP facets of the 309 perfect ICO, without affecting its characteristic icosahedral/5-fold symmetry, and then letting all atoms displace from their positions in the undistorted ICO lattice, thus introducing a moderate local structural disorder (Inset in Figure 7, bottom). The computed PDFs of the so-distorted 435-atom ICO matched the experimental PDFs in the finest detail.

3.6. Discussion on the Icosahedra Formation. Silanes added in excess as the reducing agent in a solution containing $HAuCl_4 \cdot 3H_2O$ and OY in hexane, in the ratio [OY]/[Au] = 2.5, produce mostly ultrasmall Au particles exhibiting an icosahedral structure. The average diameter measured by

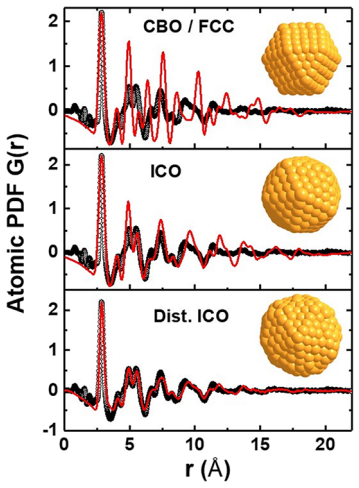

Figure 7. Comparison between experimental PDF of Au NPs prepared by reduction with [TIPS] = 62 mM at 40 °C (black circle) and different computed atomic PDFs (red line). CBO is a 309-atom cuboctahedron with an *fcc* structure, ICO is a 309-atom icosahedron, and Dist. ICO is a 435-atom distorted icosahedron. Inset: images of the structural models. Both the CBO and the 309-atom ICO have a perfect structure rendering the atomic coordination spheres/PDF peaks sharp. Although larger in size than 309-atom models, the 435-atom ICO is distorted and so exhibits somewhat smeared coordination spheres/PDF peaks in comparison to perfect CBO and ICO polyhedra.

SAXS, and confirmed by TEM, of the majority population is always 2 nm or slightly below. We have shown that compared to the standard synthesis involving [TIPS] = 62 mM at 25 °C, the size distribution was improved by three means: (i) increasing the TIPS concentration to 1 M, (ii) increasing the reaction temperature to 40 °C, or (iii) using TES as the reducing agent instead of TIPS. The effect of these three parameters was an increase of the reduction rate, avoiding the crystallization of a OY-Au(I)-Cl lamellar phase, which is in direct competition with the nucleation/growth of the Au icosahedral NPs. On the other hand, when TIPS was added in the stoichiometric amount (30 mM), the size distribution of the gold particles was very broad with a mean size around 6 nm (Figure S6). In this case, the pale-yellow solution of the Au(III) precursor turned first to a cloudy brown suspension in ∼5 min and became red dark after 8 min. Such a cloudy phase is typical of the lamellar phase, which confirms that formation of the lamellar phase during the reduction slows down the reduction and broadens the size distribution.

Thus, it is clear that the formation of OY-Au(I)-Cl throughout the reaction was found detrimental to the monodispersity of the final particles. Moreover, Figure 6b shows that its direct reduction by a large excess of silane favors the crystallization of Au NPs with an *fcc* structure, even when the silane was TES, which is a stronger reducing agent than TIPS. On the other hand, the ultrasmall particles have an icosahedral symmetry. The effect of the different parameters on the size and structure is summarized in Figure 8.

It is well-known that small Au NPs can crystallize with the icosahedral structure.[23,28,21,11,50] In the bulk state, the thermodynamic stable phase of Au has the *fcc* structure but decreasing the particle size favors first the decahedral structure and then the icosahedral structure below critical sizes.[11] Using *tert*-butyl aminoborane (TBAB) as the reducing agent, Peng et al. prepared Au NPs with different sizes in the range 2.4−9.5

https://doi.org/10.1021/acs.jpcc.2c07323
J. Phys. Chem. C 2023, 127, 3047−3058

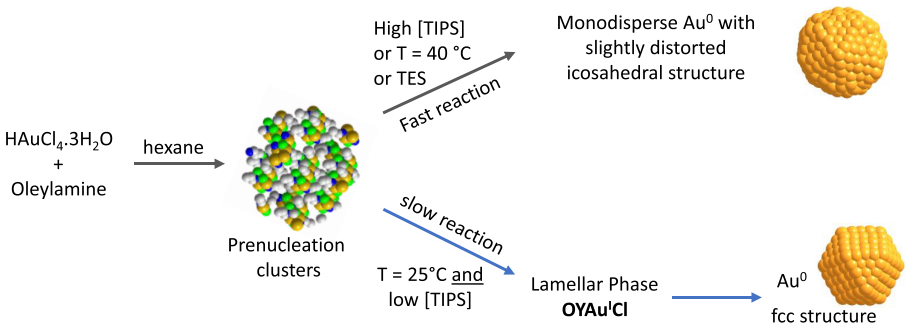

Figure 8. Schematics of the competition between the direct pathway leading to the crystallization of ultrasmall Au NPs with the icosahedral structure and the one involving the lamellar phase OY-Au(I)-Cl and leading to bigger particles with the *fcc* structure.

nm playing on the temperature of reaction in the range 2−40 °C.[22] The lower the temperature, the larger the particles obtained. The NPs with a mean diameter d_m = 2.4 nm exhibited a XRD pattern close to that described in this study with a shift in the main peak position to high q. In contrast, the particles with a diameter above 5 nm exhibited an icosahedral shape but their XRD pattern was indexed as an *fcc* structure. These particles are multitwinned particles. The effect of temperature on their size was interpreted in the framework of the classic LaMer theory: the higher the temperature, the faster the reduction rate, the higher the number of nuclei in the medium, and thus the smaller the final particles. As a matter of fact, when they decreased the temperature from 25 to 2 °C, the induction time varied from a few seconds to 5 min. The same variation of induction time was observed in our case when the TIPS concentration was varied. The reduction rate was strongly modified, the induction stage increased from a few seconds for [TIPS] = 1 M to around 3 min for [TIPS] = 62 mM. However, in our case, the particle size did not vary over such a wide size range as observed by Peng *et al.*[22] As shown in Figure 1c, by decreasing the TIPS concentration, the polydispersity increased but the mean size of the majority population of icosahedral particles was only hardly modified and their diameter remained close to 2 nm. Thus, contrary to the reaction described by Peng *et al.*, we observed that with trialkylsilanes, the nucleation of small icosahedra remains favored over their growth, even when the reduction rate is slowed down by more than one order of magnitude. An assumption that must be demonstrated in further studies is that the nucleation of the small icosahedra involves the pre-nucleation clusters evidenced by SAXS and therefore the nucleation does not depend on the TIPS concentration.

3.7. Self-Assembly of Ultrasmall NPs. The spontaneous assembly of NPs into superlattices has been intensively studied due to the peculiar collective properties.[51] It is known to be observed only with monodisperse NPs. Having a method to prepare highly monodisperse icosahedral Au NPs using [TES] = 62 mM in hand, we studied their spontaneous organization during solvent evaporation. The NPs self-assemble into crystalline superlattices once deposited on TEM grids or silicon substrates. The SAXS signal of Au NP assemblies exhibited well-defined Bragg peaks that were indexed as the first three (*hkl*) reflections of a *bcc* superlattice with a unit cell parameter a = 5.25 nm (Figure 9a). In a *bcc* structure, the distance center to center between two adjacent particles is $d_{NP-NP} = a\frac{\sqrt{3}}{2}$, taking the value of 4.55 nm in the present case. The Au core of the particles was 2.0 nm, according to SAXS. Thus, the distance edge to edge between two adjacent particles

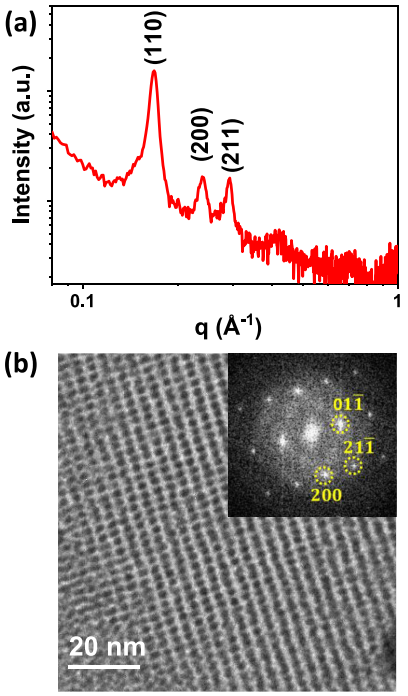

Figure 9. (a) SAXS of dried assembly of ultrasmall particles prepared with [TES] = 62 mM at 25 °C; (b) TEM image of an assembly of NPs. Inset: the corresponding FFT indexed as a *bcc* structure in the [011] zone axis.

was $e = d_{NP-NP} - d_m$ = 2.55 nm. Considering that the fully extended OY chain length is L = 2.1 nm,[52] e is in between L and 2L. NP superlattices were also observed on the TEM grids. On all the area showing a stack of a few NP layers, similar to the example in Figure 9b, the superlattice was indexed as a *bcc* structure in the [011] zone axis where the unit cell parameter is in agreement with the one determined by SAXS. The structure of NP superlattices depends on the diameter of the metal core, d_m, and on the thickness of the ligand shell coating the metal core. An *fcc* structure is generally found when the metal core is large compared to the ligand shell while a *bcc* structure is observed for small metal cores and thick ligand shells. Pansu *et al.* proposed structure diagrams of thiolated Au NP superlattices as a function of the Au core size and the number of atoms in the thiol chain or the ligand fully extended length L.[53] According to these diagrams, having a core radius $R = d_m/2$ = 1.0 nm and 18 carbon chain amine of L = 2.1 nm, the Au NP superlattice described here falls in the *bcc* structure region of Pansu's diagram, the L/R ratio of 2.1 being well

https://doi.org/10.1021/acs.jpcc.2c07323
J. Phys. Chem. C 2023, 127, 3047−3058

above the transition threshold ($L/R > 1.2$) to stabilize the *bcc* structure.

4. CONCLUSIONS

Combining *in situ* SAXS, XAS, and HE-XRD, the synthesis conditions leading to monodisperse icosahedral Au NPs with a mean diameter around 2 nm were established. A major interest of this synthesis route is the large amount of particles synthesized in a single batch thanks to the high concentration of precursor used and therefore offering the possibility of an easy scale-up. Fast reduction rate is essential to prevent the crystallization of a OY-Au(I)-Cl lamellar phase, which competes with the nucleation/growth of Au(0) NPs. Three possible reaction paths were identified: large excess of reducing agent ([TIPS] = 1 M), higher reaction temperature (T = 40 °C), or trialkylsilane with a stronger reducing strength ([TES] = 62 mM). The NPs obtained exhibit the same mean sizes and monodispersity, but the structural analysis revealed some differences on the coherence length of the NPs as a function of the reaction temperature used. It indeed increases from 1.3 nm when working at 40 °C up to 1.7 nm, close to the NP diameter, for T = 25 °C. Icosahedral NPs exhibiting a more disordered outer atomic shells are thus obtained at higher temperature.

Using silanes as the reducing agent, the degree of control over the NP size distribution and structure is excellent; however, a point concerning the nucleation/growth mechanism remains to be understood. In the framework of classical nucleation theory, one would expect a stronger variation of the mean size with the TIPS concentration or with temperature as these parameters strongly affect the reaction rate. This suggests that the pre-nucleation clusters observed in solution before the reduction are involved in the nucleation stage, imposing a fairly constant mean size. This study clarifies the model systems to be studied in the future in order to unveil the role of pre-nucleation clusters, *i.e.*, those involving a single nucleation step avoiding the formation of the lamellar OY-Au(I)-Cl phase.

■ ASSOCIATED CONTENT

Supporting Information

The Supporting Information is available free of charge at https://pubs.acs.org/doi/10.1021/acs.jpcc.2c07323.

Schematics of the microfluidic cell used for *in situ* kinetic studies; figures showing additional SAXS data, TEM images and corresponding size distribution, and PDF curves of nanoparticles; figure showing the SAXS of the intermediate lamellar phase at different temperatures; table summarizing the chemical analysis of the Au(I) intermediate lamellar phase; figures showing *in situ* XAS data and the XAS spectra of the three references used for the linear combination analysis (PDF)

■ AUTHOR INFORMATION

Corresponding Authors

Raj Kumar Ramamoorthy − *Laboratoire de Physique et Chimie des Nano-Objets, INSA Toulouse, CNRS, UMR 5215, Université Toulouse 3, F-31077 Toulouse Cedex 4, France; Laboratoire de Génie Chimique, CNRS, INP, UPS Toulouse, Université de Toulouse, 31 432 Toulouse Cedex 4, France*; Email: rajrk37@gmail.com

Lise-Marie Lacroix − *Laboratoire de Physique et Chimie des Nano-Objets, INSA Toulouse, CNRS, UMR 5215, Université Toulouse 3, F-31077 Toulouse Cedex 4, France; Institut Universitaire de France (IUF), 75005 Paris, France*; orcid.org/0000-0003-3351-7949; Email: lmlacroi@insa-toulouse.fr

Guillaume Viau − *Laboratoire de Physique et Chimie des Nano-Objets, INSA Toulouse, CNRS, UMR 5215, Université Toulouse 3, F-31077 Toulouse Cedex 4, France*; orcid.org/0000-0001-7062-4183; Email: gviau@insa-toulouse.fr

Authors

Ezgi Yildirim − *Laboratoire de Physique et Chimie des Nano-Objets, INSA Toulouse, CNRS, UMR 5215, Université Toulouse 3, F-31077 Toulouse Cedex 4, France*

Rohan Parmar − *Laboratoire de Physique et Chimie des Nano-Objets, INSA Toulouse, CNRS, UMR 5215, Université Toulouse 3, F-31077 Toulouse Cedex 4, France; Laboratoire de Génie Chimique, CNRS, INP, UPS Toulouse, Université de Toulouse, 31 432 Toulouse Cedex 4, France*

Pierre Roblin − *Laboratoire de Génie Chimique, CNRS, INP, UPS Toulouse, Université de Toulouse, 31 432 Toulouse Cedex 4, France*

Jorge A. Vargas − *Unidad Académica de Física, Universidad Autónoma de Zacatecas, 98060 Zacatecas, México*; orcid.org/0000-0002-9651-8183

Valeri Petkov − *Department of Physics, Central Michigan University, Mt. Pleasant, Michigan 48858, United States*; orcid.org/0000-0002-6392-7589

Ana Diaz − *Photon Science Division, Laboratory for Macromolecules and Bioimaging, Paul Scherrer Institute, 5232 Villigen, Switzerland*; orcid.org/0000-0003-0479-4752

Stefano Checchia − *ESRF, The European Synchrotron, 38043 Grenoble Cedex 9, France*

Isaac Rodriguez Ruiz − *Laboratoire de Génie Chimique, CNRS, INP, UPS Toulouse, Université de Toulouse, 31 432 Toulouse Cedex 4, France*

Sébastien Teychené − *Laboratoire de Génie Chimique, CNRS, INP, UPS Toulouse, Université de Toulouse, 31 432 Toulouse Cedex 4, France*; orcid.org/0000-0002-4840-1829

Complete contact information is available at: https://pubs.acs.org/10.1021/acs.jpcc.2c07323

Notes

The authors declare no competing financial interest.

■ ACKNOWLEDGMENTS

This study has been partially supported through the French national project NIMRod (ANR-21-CE09-0019-01), the EUR grant NanoX n° ANR-17-EURE-0009 in the framework of the Programme des Investissements d'Avenir". We acknowledge the Paul Scherrer Institut, Villigen, Switzerland for provision of synchrotron radiation beamtime at beamline c-SAXS of the SLS for *in situ* SAXS measurements (Proposal No. E190700304) and at beamline SuperXAS for *in situ* XAS measurements (Proposal No. 20201714). The XRD experiments were performed on beamline *ID15A* at the European Synchrotron Radiation Facility (ESRF), Grenoble, France. E.Y. thanks the Ministère de l'Enseignement Supérieur et de la Recherche et de l'Innovation for PhD funding. Angélique Gillet and Adeline Pham are warmly thanked for their help for chemical synthesis.

REFERENCES

(1) Hornyak, G. L.; Dutta, J.; Tibbals, H. F.; Rao, A.*Introduction to Nanoscience*, 1st ed.; CRC Press: 2008, DOI: 10.1201/b12835.

(2) Polte, J. Fundamental Growth Principles of Colloidal Metal Nanoparticles – a New Perspective. *CrystEngComm* **2015**, *17*, 6809–6830.

(3) Whitehead, C. B.; Finke, R. G. Particle Formation Mechanisms Supported by in Situ Synchrotron XAFS and SAXS Studies: A Review of Metal, Metal-Oxide, Semiconductor and Selected Other Nanoparticle Formation Reactions. *Mater. Adv.* **2021**, *2*, 6532–6568.

(4) Kwon, K.; Lee, K. Y.; Lee, Y. W.; Kim, M.; Heo, J.; Ahn, S. J.; Han, S. W. Controlled Synthesis of Icosahedral Gold Nanoparticles and Their Surface-Enhanced Raman Scattering Property. *J. Phys. Chem. C* **2007**, *111*, 1161–1165.

(5) Sakthivel, N. A.; Theivendran, S.; Ganeshraj, V.; Oliver, A. G.; Dass, A. Crystal Structure of Faradaurate-279: Au $_{279}$ (SPh- *t* Bu) $_{84}$ Plasmonic Nanocrystal Molecules. *J. Am. Chem. Soc.* **2017**, *139*, 15450–15459.

(6) Mikami, Y.; Dhakshinamoorthy, A.; Alvaro, M.; García, H. Catalytic Activity of Unsupported Gold Nanoparticles. *Catal. Sci. Technol.* **2013**, *3*, 58–69.

(7) Maurer, J. H. M.; González-García, L.; Reiser, B.; Kanelidis, I.; Kraus, T. Sintering of Ultrathin Gold Nanowires for Transparent Electronics. *ACS Appl. Mater. Interfaces* **2015**, *7*, 7838–7842.

(8) Maurer, J. H. M.; González-García, L.; Reiser, B.; Kanelidis, I.; Kraus, T. Templated Self-Assembly of Ultrathin Gold Nanowires by Nanoimprinting for Transparent Flexible Electronics. *Nano Lett.* **2016**, *16*, 2921–2925.

(9) Plant, S. R.; Cao, L.; Palmer, R. E. Atomic Structure Control of Size-Selected Gold Nanoclusters during Formation. *J. Am. Chem. Soc.* **2014**, *136*, 7559–7562.

(10) Wells, D. M.; Rossi, G.; Ferrando, R.; Palmer, R. E. Metastability of the Atomic Structures of Size-Selected Gold Nanoparticles. *Nanoscale* **2015**, *7*, 6498–6503.

(11) Baletto, F.; Ferrando, R. Structural Properties of Nanoclusters: Energetic, Thermodynamic, and Kinetic Effects. *Rev. Mod. Phys.* **2005**, *77*, 371–423.

(12) Nassereddine, A.; Wang, Q.; Loffreda, D.; Ricolleau, C.; Alloyeau, D.; Louis, C.; Delannoy, L.; Nelayah, J.; Guesmi, H. Revealing Size Dependent Structural Transitions in Supported Gold Nanoparticles in Hydrogen at Atmospheric Pressure. *Small* **2021**, *17*, 2104571.

(13) Ramamoorthy, R. K.; Soulantica, K.; Del Rosal, I.; Arenal, R.; Decorse, P.; Piquemal, J.-Y.; Chaudret, B.; Poteau, R.; Viau, G. Ruthenium Icosahedra and Ultrathin Platelets: The Role of Surface Chemistry on the Nanoparticle Structure. *Chem. Mater.* **2022**, *34*, 2931–2944.

(14) Negishi, Y.; Nakazaki, T.; Malola, S.; Takano, S.; Niihori, Y.; Kurashige, W.; Yamazoe, S.; Tsukuda, T.; Häkkinen, H. A Critical Size for Emergence of Nonbulk Electronic and Geometric Structures in Dodecanethiolate-Protected Au Clusters. *J. Am. Chem. Soc.* **2015**, *137*, 1206–1212.

(15) Barmparis, G. D.; Lodziana, Z.; Lopez, N.; Remediakis, I. N. Nanoparticle Shapes by Using Wulff Constructions and First-Principles Calculations. *Beilstein J. Nanotechnol.* **2015**, *6*, 361–368.

(16) Yang, F.; Ye, J.; Yuan, Q.; Yang, X.; Xie, Z.; Zhao, F.; Zhou, Z.; Gu, L.; Wang, X. Ultrasmall Pd-Cu-Pt Trimetallic Twin Icosahedrons Boost the Electrocatalytic Performance of Glycerol Oxidation at the Operating Temperature of Fuel Cells. *Adv. Funct. Mater.* **2020**, *30*, 1908235.

(17) Wang, W.; Zhou, S.; Shen, M.; Hood, Z. D.; Xiao, K.; Xia, Y. Facile Synthesis of Silver Icosahedral Nanocrystals with Uniform and Controllable Sizes. *ChemNanoMat* **2018**, *4*, 1071–1077.

(18) Zhou, W.; Wu, J.; Yang, H. Highly Uniform Platinum Icosahedra Made by Hot Injection-Assisted GRAILS Method. *Nano Lett.* **2013**, *13*, 2870–2874.

(19) Zhao, M.; Holder, J.; Chen, Z.; Xie, M.; Cao, Z.; Chi, M.; Xia, Y. Facile Synthesis of Pt Icosahedral Nanocrystals with Controllable Sizes for the Evaluation of Size-Dependent Activity toward Oxygen Reduction. *ChemCatChem* **2019**, *11*, 2458–2463.

(20) Huang, L.; Shan, A.; Li, Z.; Chen, C.; Wang, R. Phase Formation, Magnetic and Optical Properties of Epitaxially Grown Icosahedral Au@Ni Nanoparticles with Ultrathin Shells. *CrystEngComm* **2013**, *15*, 2527.

(21) Wang, H.; Zhou, S.; Gilroy, K. D.; Cai, Z.; Xia, Y. Icosahedral Nanocrystals of Noble Metals: Synthesis and Applications. *Nano Today* **2017**, *15*, 121–144.

(22) Peng, S.; Lee, Y.; Wang, C.; Yin, H.; Dai, S.; Sun, S. A Facile Synthesis of Monodisperse Au Nanoparticles and Their Catalysis of CO Oxidation. *Nano Res.* **2008**, *1*, 229–234.

(23) Vargas, J. A.; Petkov, V.; Nouh, E. S. A.; Ramamoorthy, R. K.; Lacroix, L.-M.; Poteau, R.; Viau, G.; Lecante, P.; Arenal, R. Ultrathin Gold Nanowires with the Polytetrahedral Structure of Bulk Manganese. *ACS Nano* **2018**, *12*, 9521–9531.

(24) Abécassis, B.; Testard, F.; Kong, Q.; Francois, B.; Spalla, O. Influence of Monomer Feeding on a Fast Gold Nanoparticles Synthesis: Time-Resolved XANES and SAXS Experiments. *Langmuir* **2010**, *26*, 13847–13854.

(25) Leffler, V.; Ehlert, S.; Förster, B.; Dulle, M.; Förster, S. Nanoparticle Heat-Up Synthesis: In Situ X-Ray Diffraction and Extension from Classical to Nonclassical Nucleation and Growth Theory. *ACS Nano* **2021**, *15*, 840–856.

(26) Kashchiev, D.; van Rosmalen, G. M. Review: Nucleation in Solutions Revisited. *Cryst. Res. Technol.* **2003**, *38*, 555–574.

(27) Watzky, M. A.; Finke, R. G. Transition Metal Nanocluster Formation Kinetic and Mechanistic Studies. A New Mechanism When Hydrogen Is the Reductant: Slow, Continuous Nucleation and Fast Autocatalytic Surface Growth. *J. Am. Chem. Soc.* **1997**, *119*, 10382–10400.

(28) Ramamoorthy, R. K.; Yildirim, E.; Barba, E.; Roblin, P.; Vargas, J. A.; Lacroix, L.-M.; Rodriguez-Ruiz, I.; Decorse, P.; Petkov, V.; Teychené, S.; Viau, G. The Role of Pre-Nucleation Clusters in the Crystallization of Gold Nanoparticles. *Nanoscale* **2020**, *12*, 16173–16188.

(29) Mikhlin, Y.; Likhatski, M.; Karacharov, A.; Zaikovski, V.; Krylov, A. Formation of Gold and Gold Sulfide Nanoparticles and Mesoscale Intermediate Structures in the Reactions of Aqueous HAuCl4 with Sulfide and Citrate Ions. *Phys. Chem. Chem. Phys.* **2009**, *11*, 5445–5454.

(30) Mikhlin, Y.; Karacharov, A.; Likhatski, M.; Podlipskaya, T.; Zubavichus, Y.; Veligzhanin, A.; Zaikovski, V. Submicrometer Intermediates in the Citrate Synthesis of Gold Nanoparticles: New Insights into the Nucleation and Crystal Growth Mechanisms. *J. Colloid Interface Sci.* **2011**, *362*, 330–336.

(31) Loh, N. D.; Sen, S.; Bosman, M.; Tan, S. F.; Zhong, J.; Nijhuis, C. A.; Král, P.; Matsudaira, P.; Mirsaidov, U. Multistep Nucleation of Nanocrystals in Aqueous Solution. *Nat. Chem.* **2017**, *9*, 77–82.

(32) De Yoreo, J. J.; Gilbert, P. U. P. A.; Sommerdijk, N. A. J. M.; Penn, R. L.; Whitelam, S.; Joester, D.; Zhang, H.; Rimer, J. D.; Navrotsky, A.; Banfield, J. F.; Wallace, A. F.; Michel, F. M.; Meldrum, F. C.; Cölfen, H.; Dove, P. M. Crystallization by Particle Attachment in Synthetic, Biogenic, and Geologic Environments. *Science* **2015**, *349*, aaa6760.

(33) Liu, Z.; Zhang, Z.; Wang, Z.; Jin, B.; Li, D.; Tao, J.; Tang, R.; De Yoreo, J. J. Shape-Preserving Amorphous-to-Crystalline Transformation of CaCO3 Revealed by in Situ TEM. *Proc. Natl. Acad. Sci.* **2020**, *117*, 3397–3404.

(34) Fleury, B.; Neouze, M.-A.; Guigner, J.-M.; Menguy, N.; Spalla, O.; Gacoin, T.; Carriere, D. Amorphous to Crystal Conversion as a Mechanism Governing the Structure of Luminescent YVO4:Eu Nanoparticles. *ACS Nano* **2014**, *8*, 2602–2608.

(35) Baumgartner, J.; Ramamoorthy, R. K.; Freitas, A. P.; Neouze, M.-A.; Bennet, M.; Faivre, D.; Carriere, D. Self-Confined Nucleation of Iron Oxide Nanoparticles in a Nanostructured Amorphous Precursor. *Nano Lett.* **2020**, *20*, 5001–5007.

(36) Gebauer, D.; Gunawidjaja, P. N.; Ko, J. Y. P.; Bacsik, Z.; Aziz, B.; Liu, L.; Hu, Y.; Bergström, L.; Tai, C.-W.; Sham, T.-K.; Edén, M.;

Hedin, N. Proto-Calcite and Proto-Vaterite in Amorphous Calcium Carbonates. *Angew. Chem., Int. Ed.* **2010**, *49*, 8889−8891.
(37) Pschunder, F.; Puig, J.; Giovanetti, L. J.; Huck-Iriart, C.; Requejo, F. G.; Buceta, D.; Hoppe, C. E.; Ramallo-López, J. M. New Insights into the Growth Mechanism of Ultrathin Au Nanowires from Combined in Situ EXAFS and SAXS Studies. *J. Phys. Chem. C* **2018**, *122*, 29051−29061.
(38) Gavira, J. A.; Rodriguez-Ruiz, I.; Martinez-Rodriguez, S.; Basu, S.; Teychené, S.; McCarthy, A. A.; Mueller-Dieckman, C. Attaining Atomic Resolution from It in Situ Data Collection at Room Temperature Using Counter-Diffusion-Based Low-Cost Microchips. *Acta Crystallogr., Sect. D: Struct. Biol.* **2020**, *76*, 751−758.
(39) Rodríguez-Ruiz, I.; Charton, S.; Radajewski, D.; Bizien, T.; Teychené, S. Ultra-Fast Precipitation of Transient Amorphous Cerium Oxalate in Concentrated Nitric Acid Media. *CrystEngComm* **2018**, *20*, 3302−3307.
(40) Lu, Z.; McMahon, J.; Mohamed, H.; Barnard, D.; Shaikh, T. R.; Mannella, C. A.; Wagenknecht, T.; Lu, T.-M. Passive Microfluidic Device for Submillisecond Mixing. *Sens. Actuators, B* **2010**, *144*, 301−309.
(41) Vaughan, G. B. M.; Baker, R.; Barret, R.; Bonnefoy, J.; Buslaps, T.; Checchia, S.; Duran, D.; Fihman, F.; Got, P.; Kieffer, J.; Kimber, S. A. J.; Martel, K.; Morawe, C.; Mottin, D.; Papillon, E.; Petitdemange, S.; Vamvakeros, A.; Vieux, J.-P.; Di Michiel, M. ID15A at the ESRF − a Beamline for High Speed *Operando* X-Ray Diffraction, Diffraction Tomography and Total Scattering. *J. Synchrotron Radiat.* **2020**, *27*, 515−528.
(42) Olsson, P. A. T. Transverse Resonant Properties of Strained Gold Nanowires. *J. Appl. Phys.* **2010**, *108*, No. 034318.
(43) Thompson, A. P.; Aktulga, H. M.; Berger, R.; Bolintineanu, D. S.; Brown, W. M.; Crozier, P. S.; In't Veld, P. J.; Kohlmeyer, A.; Moore, S. G.; Nguyen, T. D.; Shan, R.; Stevens, M. J.; Tranchida, J.; Trott, C.; Plimpton, S. J. LAMMPS - a Flexible Simulation Tool for Particle-Based Materials Modeling at the Atomic, Meso, and Continuum Scales. *Comput. Phys. Commun.* **2022**, *271*, No. 108171.
(44) Prasai, B.; Wilson, A. R.; Wiley, B. J.; Ren, Y.; Petkov, V. On the Road to Metallic Nanoparticles by Rational Design: Bridging the Gap between Atomic-Level Theoretical Modeling and Reality by Total Scattering Experiments. *Nanoscale* **2015**, *7*, 17902−17922.
(45) Beaucage, G. Small-Angle Scattering from Polymeric Mass Fractals of Arbitrary Mass-Fractal Dimension. *J. Appl. Crystallogr.* **1996**, *29*, 134−146.
(46) Lu, X.; Tuan, H.-Y.; Korgel, B. A.; Xia, Y. Facile Synthesis of Gold Nanoparticles with Narrow Size Distribution by Using AuCl or AuBr as the Precursor. *Chem. − Eur. J.* **2008**, *14*, 1584−1591.
(47) Loubat, A.; Lacroix, L.-M.; Robert, A.; Impéror-Clerc, M.; Poteau, R.; Maron, L.; Arenal, R.; Pansu, B.; Viau, G. Ultrathin Gold Nanowires: Soft-Templating versus Liquid Phase Synthesis, a Quantitative Study. *J. Phys. Chem. C* **2015**, *119*, 4422−4430.
(48) Sugie, A.; Somete, T.; Kanie, K.; Muramatsu, A.; Mori, A. Triethylsilane as a Mild and Efficient Reducing Agent for the Preparation of Alkanethiol-Capped Gold Nanoparticles. *Chem. Commun.* **2008**, *33*, 3882.
(49) Cui, F.; Yu, Y.; Dou, L.; Sun, J.; Yang, Q.; Schildknecht, C.; Schierle-Arndt, K.; Yang, P. Synthesis of Ultrathin Copper Nanowires Using Tris(Trimethylsilyl)Silane for High-Performance and Low-Haze Transparent Conductors. *Nano Lett.* **2015**, *15*, 7610−7615.
(50) Kloppenburg, J.; Pedersen, A.; Laasonen, K.; Caro, M. A.; Jónsson, H. Reassignment of Magic Numbers for Icosahedral Au Clusters: 310, 564, 928 and 1426. *Nanoscale* **2022**, *14*, 9053−9060.
(51) Boles, M. A.; Engel, M.; Talapin, D. V. Self-Assembly of Colloidal Nanocrystals: From Intricate Structures to Functional Materials. *Chem. Rev.* **2016**, *116*, 11220−11289.
(52) Mourdikoudis, S.; Liz-Marzán, L. M. Oleylamine in Nanoparticle Synthesis. *Chem. Mater.* **2013**, *25*, 1465−1476.
(53) Pansu, B.; Goldmann, C.; Constantin, D.; Impéror-Clerc, M.; Sadoc, J.-F. Softness-Driven Complexity in Supercrystals of Gold Nanoparticles. *Soft Matter* **2021**, *17*, 6461−6469.

https://doi.org/10.1021/acs.jpcc.2c07323
J. Phys. Chem. C 2023, 127, 3047−3058